공학석사학위논문

Flexible Asymmetric Supercapacitor Twisted from Carbon Fiber/MnO_2 and Carbon Fiber/MoO_3

탄소 섬유/금속 산화물을 감은 형태의 유연한 비대칭 슈퍼캐패시터

2017년 2월

서울대학교 대학원

화학생물공학부

노 정 철

Flexible Asymmetric Supercapacitor Twisted from Carbon Fiber/MnO_2 and carbon Fiber/MoO_3	2017	나정철	↑ 3cm ↓	↑ 4cm ↓	↑ 2.5cm ↓	↑ 2cm ↓

Abstract

Flexible Asymmetric Supercapacitor Twisted from Carbon Fiber/MnO_2 and Carbon Fiber/MoO_3

Jungchul Noh

School of Chemical and Biological Engineering

The Graduate School

Seoul National University

Fiber-shaped supercapacitors are promising energy storage devices for future flexible and portable electronics. In this study, we report a fiber-shaped asymmetric supercapacitor (ASC) device made with the metal oxides having a large work function difference, directly grown on a flexible and conductive carbon fiber (CF) substrate. Specifically, carbon fiber/MnO_2 (CF/MnO_2) and carbon fiber/MoO_3 (CF/MoO_3) were fabricated using a simple electrodeposition method. The all-solid-state fiber-shaped ASC device was then assembled with CF/MnO_2 as the positive electrode and CF/MoO_3 as the negative electrode. The large work function difference between the metal oxides and the high conductivity of the CF substrate provided the ASC device with remarkable performance. In particular, it exhibited capacitance of 4.86 mF cm^{-2} and a wide operating voltage window of 2.0 V, which resulted in an excellent energy density of 2.70 μWh cm^{-2} and a power density of 0.53 mW cm^{-2}. Also, it readily tolerated 3000 cycles of

electrochemical testing and extreme mechanical deformation. Consequently, the outstanding performance and stability of the fiber-shaped ASC device shows great potential for future energy storage systems.

Keyword: Fiber supercapacitor, Asymmetric supercapacitor, work function, MnO_2, and MoO_3

Student number: 2015–21018

List of Abbreviations

AC: Alternating Current

ASC: Asymmetric Supercapacitor

CF: Carbon Fiber

CF/MnO_2 Carbon Fiber coated by Manganese Dioxide

CF/MoO_3: Carbon Fiber coated by Molybdenum Trioxide

CNT: Carbon Nanotube

CV: Cyclic Voltammetry

EDLC: Electric Double Layer Capacitance

EDS: Energy-Dispersive X-ray Spectroscopy

EDTA: Ethylenediaminetetraacetic acid

EIS: Electrochemical Impedance Spectroscopy

ESR: Equivalent Series Resistance

FE-SEM: Field-Emission Scanning Electron Microspocy

GCD: Galvanostatic Charge-Discharge

LED: Light-Emitting Diode

MnO_2 manganese Dioxide

$Mn(Ac)_2 \cdot 4H_2O$: Manganese (Ⅱ) Acetate Tetrahydrate

MoO_3: Molybdenum Trioxide

Na_2MoO_4: Sodium Molybdate

PVA: Poly(vinyl alcohol)

Q: Charge

Q_+: Charge of positive electrode

Q_-: Charge of negative electrode

R_{CT}: Charge Transfer Resistance

S: Surface Area

V: Operating Voltage Window

XPS: X-ray Photoelectron Spectroscopy

XRD: X-ray diffraction

List of Figures

Figure 5. EDS analysis of (a) CF/MnO_2 and (b) CF/MoO_3, respectively.

Figure 6. (a) Wide-scan XPS spectra of CF/MnO_2 and CF/MoO_3. XPS spectra of (b) Mn 2p level for CF/MnO_2 and (c) Mo 3d level for CF/MoO_3. (d) XRD patterns of CF/MnO_2, CF/MoO_3, and CF, respectively.

Figure 7. (a) Cyclic voltammetry (CV) curves of the active materials in three electrode system with a scan rate of 50 mV s^{-1}. CV curves of (b) CF/MnO_2 and (c) CF/MoO_3 at various scan rates. Galvanostatic charge-discharge (GCD) curves of (d) CF/MnO_2 and (e) CF/MoO_3 at various current densities. (f) Areal capacitance of the active materials at different current densities.

Figure 8. CV curves of carbon fiber (CF) with varying scan rates in three electrode system

Figure 9. CV curves of CF/MnO_2 electrodes with varying reaction time in three electrode system. CV curves of CF/MnO_2 with reaction time of (a) 5, (b) 15, and (c) 20 min, respectively. (d) Areal capacitance of the various CF/MnO_2 materials.

Figure 10. CV curves of CF/MoO_3 electrodes with varying reaction time in three electrode system. CV curves of CF/MoO_3 with reaction time of (a) 5, (b) 15, and (c) 20 min, respectively. (d) Areal capacitance of the various CF/MoO_3 materials.

Figure 11. (a-b) CV curves of the assembled all-solid-state fiber-shaped asymmetric supercapacitor (ASC) device with various cell voltages and scan rates. (c-d) GCD curves of the ASC device with different voltage windows and current densities. (e) Areal capacitance of the ASC device with different current densities. (f) Electrochemical impedance spectroscopy (EIS) analysis of the ASC device.

Figure 12. Areal capacitances of the fiber-shaped ASC device with increasing the operating voltage window.

Figure 13. Digital photograph of (a) CF/MnO_2//CF/MoO_3 fiber-shaped ASC device. (b) Photograph of the ASC device lightning red LED. (c) Long-term cycling test of the ASC device with a current density of 5 mA cm^{-2}. (d) CV curves of the ASC device with different bending angles.

Figure 14. (a, b) Cyclic voltammetry (CV) and galvanostatic charge discharge (GCD) curves of the symmetric supercapacitor assembled by CF/MnO_2. (c, d) CV and GCD curves of the symmetric supercapacitor constructed by CF/MoO_3. (e, f) The areal capacitance and Ragone plot of the symmetric supercapacitors.

Figure 15. Ragone plot of CF/MnO_2//CF/MoO_3 fiber-shaped ASC device compared to various fiber-based supercapacitor devices.

List of Tables

Contents

Chapter 1. Introduction

1.1 Fiber-shaped supercapacitors

Modern electronics are trending toward flexible, wearable, and portable devices while simultaneously requiring high performance [1–6]. To power them, it is indispensable to develop energy storage devices possessing these attributes. Supercapacitors have attracted much attention as power sources due to their fast charge-discharge rate, high power density, and long cycling life [7,8]. Compared with the conventional two-dimensional (2D) planar configuration, one-dimensional (1D) fiber-shaped supercapacitors are particularly promising for energy storage devices due to their light weight and flexibility [9.10]. These benefits are often achieved using conductive carbon-based fibers such as graphene fibers, carbon nanotubes (CNTs), and carbon fibers (CFs) [7,8,9]. However, fiber-shaped supercapacitors based on pure carbon materials deliver low energy density unless they sacrifice power density, thus restricting their potential application [11,12]. As such, their energy density must be improved for future energy-related applications.

1.2. Asymmetric supercapacitors

Effective approaches to achieve a high energy density are to maximize the operating voltage window and the capacitance [7,13]. Organic and ionic electrolytes are often used to extend the operating voltage window, although they suffer from toxicity, poor ionic conductivity, and short cycle life [14,15]. Alternatively, asymmetric supercapacitors (ASCs) based on aqueous electrolytes use active materials that work in different operating voltage windows, can take advantage of high ionic conductivities, and are more environmentally benign [16–18]. Using active materials that display pseudocapacitive behavior further enhances the capacitance of ASCs due to their redox chemistry [2]. Consequently, ASCs can increase the operating voltage window and capacitance of active materials, resulting in a significant enhancement of the energy density.

1.3. Active materials for asymmetric supercapacitors

Among the various kinds of active materials for ASCs, metal oxides have been widely investigated because their redox reactions enable high specific capacitances [19–22]. However, their poor conductivities, low stabilities, and insufficient rate capabilities deteriorate the performance of supercapacitors made from them [23,24]. To overcome these drawbacks, many researchers have combined metal oxides with conductive carbon-based fibers. For example, Xu *et al*. fabricated MnO_2-coated CNT fibers and assembled a wire-shaped ASC with pristine CNT [25]. Liu *et al*. synthesized a $ZnCo_2O_4$ nanowire array/CF electrode to construct a planar-integrated fiber-shaped supercapacitor [26]. However, the relatively narrow operating voltage windows and insufficient capacitances were not suitable for energy storage systems. Therefore, a rational design is required for fiber-shaped supercapacitors to achieve the desired high performance.

For this purpose, molybdenum trioxide (MoO_3) is an excellent material for the negative electrode of an ASC due to its low cost, the mixed valence states of Mo, and high work function (6.9 eV) [27,28]. The multiple valence states provide active sites for improving the electrochemical performance [29]. A larger work function difference between the positive and negative electrodes widens the operating voltage window of ASCs [30]. In this regard, manganese dioxide (MnO_2) is a reasonable choice for active material for the positive

electrode of an ASC due to its lower work function (4.4 eV) [31]. Additionally, it has the advantages of low cost, environmental friendliness, and a high theoretical capacitance of 1380 F g^{-1} [32,33]. Thus, fiber-shaped ASCs assembled with the two metal oxides-based carbon materials could have a high electrochemical performance due to the improved conductivity and large work function difference.

1.4. Objective and Outlines of the Study

1.4.1. Objective

Herein, the all-solid-state fiber-shaped ASC device based on CF coated by MnO_2 (CF/MnO_2) and MoO_3 (CF/MoO_3) was demonstrated to have excellent electrochemical performance. The two metal oxides, which provided the large work function difference, were directly grown on the conductive CF substrate *via* a facile electrodeposition method. The petal-like architecture of MnO_2 and bamboo-like architecture of MoO_3 provided large active sites, which made ready access of electrolytes to electrodes. Also, the optimal synthetic conditions were identified to elicit the highest-performing fiber-shaped ASC device. To our knowledge, this is the first report that describes a fiber-shaped ASC device based on the metal oxides having the largest work function difference grown directly on a flexible and conductive CF substrate. The ASC device had a high capacitance of 4.86 mF cm^{-2} at a current density of 0.5 mA cm^{-2}, with an enhanced operating voltage window of 2.0 V. The corresponding energy density and power density were 2.70 μWh cm^{-2} and 0.53 mW cm^{-2}, respectively.

1.4.2. Outlines

1) In this work, a simple fabrication procedure to construct unique, active material architectures was investigated. Complex manufacturing procedures are often required to make novel active materials, thus, presenting challenges to precisely control their architectures. However, in this study, a simple electrodeposition method was used to successfully coat a commercially available carbon fiber (CF) substrate with MnO_2 and MoO_3 to provide unique morphologies. Specifically, CF/MnO_2 and CF/MoO_3 were fabricated with petal-like and bamboo-like morphologies and relatively uniform depositions over a short electrodeposition time. The proposed approach provides a new fabrication method for novel active materials.

2) To our knowledge, this is the first report of a fiber-shaped asymmetric supercapacitor (ASC) device made with metal oxides having large work function differences, grown directly on a flexible and conductive CF substrate. The large work function difference between the two electrodes enlarged the operating voltage window to 2.0 V. Also, the pseudocapacitive behavior of the metal oxides enabled the ASC device to achieve a high capacitance combined with the electric double-layer contribution of the conductive CF substrate. As a result, a remarkable energy density was delivered even at a high power density. Specifically, when the current density was increased from 0.5 to 5 mA cm^{-2}, the

energy density of the ASC device decreased from 2.70 to 1.78 μWh cm^{-2}, while the power density increased from 0.53 to 6.22 mW cm^{-2}. Such high-performances of the assembled ASC device provides deep insight into an effective approach for future fiber-shaped energy storage devices.

3) Finally, the viability of the ASC device for practical applications was examined. The high electrochemical performance of the ASC device was demonstrated by illuminating a red light-emitting diode (LED) bulb. Due to the large operating voltage window and high capacitance, the charged ASC device could deliver sufficient energy to light the 1.6 V LED bulb. The superior electrochemical performance retained 89% of the initial capacitance, even after 3000 cycles of galvanostatic charging and discharging. Moreover, the ASC device showed high flexibility and endurance against mechanical deformation; bending at different angles had little effect on the capacitance. The fabricated ASC device shows great potential for practical energy storage, as demonstrated by its outstanding performance and stability.

Chapter 2. Experimental

2.1. Materials

Manganese (II) acetate tetrahydrate ($Mn(Ac)_2 \cdot 4H_2O$), sodium molybdate (Na_2MoO_4), ethylenediaminetetraacetic acid (EDTA), ammonium acetate, Poly(vinyl alcohol) (PVA, Mw 85000), and potassium hydroxide (KOH) were purchased from Aldrich Chemical Co. and used without further purification. Carbon fiber (T300B) was obtained from Toray Co. and used as received

2.2. Preparation of CF/MnO_2 as the positive electrode

CF/MnO_2 was fabricated using an electrodeposition method in a three electrode system. Firstly, CF (Toray. T300B) immersed in HCl solution (1 M) was heated at 70 ℃ for 6 h and washed with distilled water several times. Then, three electrode system was constructed with the CF as a working electrode, Pt wire as a counter electrode, Ag/AgCl as a reference electrode, and $Mn(Ac)_2$ (0.1 M) as an electrolyte, respectively. In the three electrode system, MnO_2 was grown on the CF with the constant current of 20 mA at 70 ℃ for different reaction time (5, 10, 15, and 20 min) and subsequently dried in oven for overnight.

2.3. Preparation of CF/MoO_3 as the negative electrode

CF/MoO_3 was fabricated using an electrodeposition method in a three electrode configuration. Prior to the fabrication, CF submerged in HCl solution (1 M) was heated at 70 ℃ for 6 h and washed with distilled water several times. Then, three electrode configuration was established with the CF as a working electrode, Pt wire as a counter electrode, and Ag/AgCl as a reference electrode, respectively. Also, an electrolyte solution was prepared with the mixture of Na_2MoO_4 (0.1 M), EDTA (0.1 M), and ammonium acetate (0.1 M). In the three electrode configuration, MoO_3 was grown on the surface of CF with the constant voltage of –2 V at 70 ℃ for different reaction time (5, 10, 15, and 20 min) and finally dried in oven for overnight.

2.4 Construction of the fiber-shaped supercapacitor

To assemble the all-solid-state fiber-shaped ASC device, CF/MnO_2 and CF/MoO_3 were used as a positive and negative electrode, respectively. According to the capacitance measured in three electrode system, the areal ratio of CF/MnO_2 and CF/MoO_3 was set to 1:3 to satisfy the charge balance of two electrodes. Subsequently, the electrodes were separated by PVA/KOH gel electrolyte. Specifically, PVA (10 wt%) solution was dropped on CF/MnO_2 and solidified at 60 °C for overnight. Then, the PVA coated CF/MnO_2 was dipped in KOH (1 M) solution for 1 min. On the other hand, PVA solution was dropped on the CF/MoO_3 without the drying procedure. After the two electrodes were twisted, the ASC device was immersed in KOH (1 M) solution and dried for overnight.

2.5 Characterizations and electrochemical measurements

The structural morphologies and elemental mapping of the resulting materials were obtained by FE-SEM (JSM–6700F, JEOL) installed with an energy dispersive X-ray spectrometer (INCA energy). The surface chemical states were investigated by XPS (Sigma Probe, Thermo-VG, UK). The crystal structures were examined using a SmartLab X-ray diffractometer (Rigaku, Japan) with Cu Kα radiation source (λ = 1.541 Å) in the 2θ range of 10–80° at 10° min^{-1}. CV, GCD, and EIS measurements were conducted employing an electrochemical workstation (Zahner Elektrik). The electrochemical properties were examined by presuming the active materials of fiber bundles as a cylindrical shape. The capacitance was calculated using the following equations:

$$C = \frac{1}{S \times V} \int I \, dV \quad \text{(from CV curves)} \tag{1}$$

$$C = \frac{I \times \Delta t}{S \times V} \quad \text{(from GCD curves)} \tag{2}$$

where C is the areal capacitance, S is the surface area of the active materials, I is the discharging current, V is the voltage, ΔV is the operating voltage window, Δt is the discharging time. Also, the energy density and power density were calculated by the following relationship:

$$E = \frac{1}{2} C \Delta V^2 \tag{3}$$

$$P = \frac{E}{\Delta t} \tag{4}$$

where E is the energy density and P is the power density, respectively.

Chapter 3. Results and discussion

3.1 Fabrication of the positive and negative electrodes

3.1.1. Overall procedure

Figure 1 depicts a schematic illustration of the overall procedure used to assemble the ASC device based on CF/MnO_2 as the positive electrode and CF/MoO_3 as the negative electrode. In addition to the flexible and conductive CF substrate, MnO_2 and MoO_3 were chosen as the positive and negative electrode materials due to their high electrochemical performances and large work function difference (**Figure 2**) [30,31]. Specifically, CF/MnO_2 and CF/MoO_3 were fabricated using a facile electrodeposition method. The CF was first pre-treated with H_2SO_4 at 70 °C to remove the sizing agent on the surface of the fibers. Then, MnO_2 or MoO_3 was grown on the CF substrate using three electrode configuration with CF as the working electrode, Pt wire as the counter electrode, and Ag/AgCl as the reference electrode. The MnO_2 was decorated on the surface of CF at a constant current of 20 mA for 10 min in a manganese acetate ($Mn(Ac)_2$) solution. The MoO_3 was coated on the surface of the CF at a

constant voltage of –2 V for 10 min in a sodium molybdate (Na_2MoO_4) solution. The resulting active materials were assembled as the electrodes for the fiber-shaped ASC device.

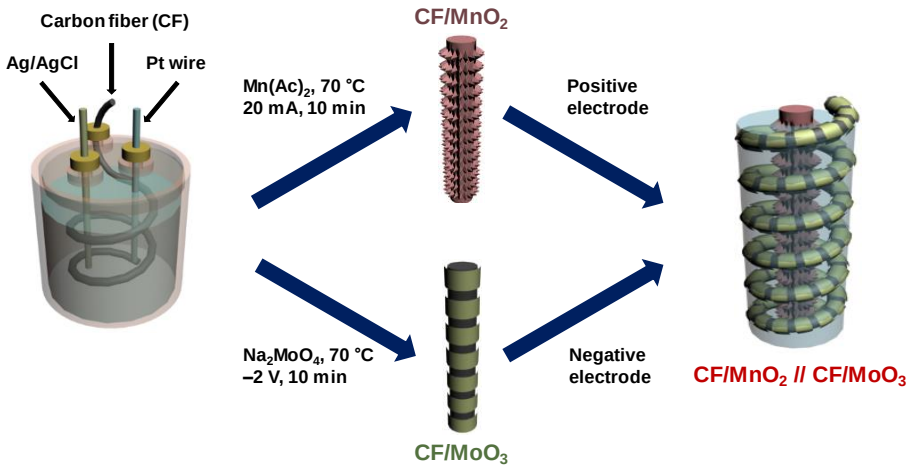

Figure 1. Schematic illustration of the assembled all-solid-state fiber-shaped asymmetric supercapacitor (ASC) device based on CF/MnO_2 as the positive electrode and CF/MoO_3 as the negative electrode, respectively.

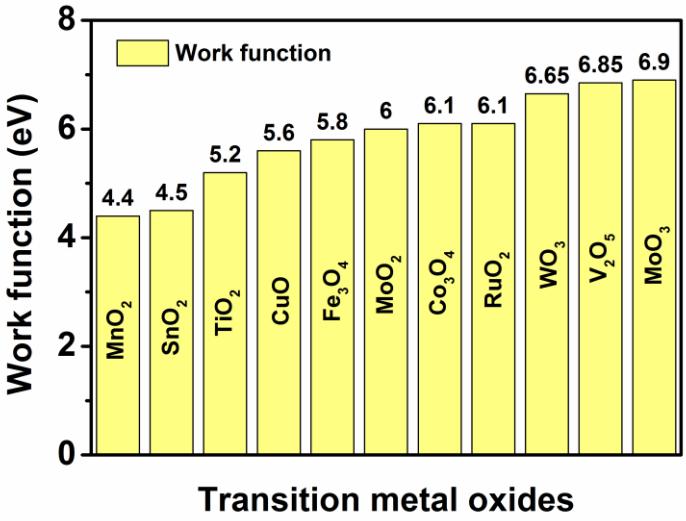

Figure 2. Work function of various transition metal oxides. Among them, MnO_2 and MoO_3 were chosen as the positive and negative electrode materials, respectively, due to the largest work function difference between the two metal oxides.

3.1.2. Characterizations

The detailed morphologies and elemental mapping of the CF, CF/MnO_2, and CF/MoO_3 samples were investigated by field-emission scanning electron microscopy (FE-SEM) equipped with energy-dispersive X-ray spectroscopy (EDS) as shown in **Figure 3**. The pristine CF had a cylindrical shape with an average diameter of *ca*. 7 μm and was composed of only C elements as revealed by cross sectional elemental mapping. However, the surface morphology and elemental compositions were changed by introducing MnO_2 and MoO_3 to the CF substrate. To examine the growth of the metal oxides on the CF, the two active materials were fabricated by varying the electrodeposition time (5, 10, 15, and 20 min) at a constant current of 20 mA (**Figure 4**). The MnO_2 architecture evolved from a petal-like architecture to micronodules with increasing electrodeposition time. The petal-like MnO_2 first grew vertically on the CF substrate at a short reaction time, but the continued growth over longer times resulted in the formation of MnO_2 micronodules having a diameter of *ca*. 1–2 μm. Under the experimental conditions, the optimal reaction time for CF/MnO_2 was 10 min, which provided a uniform MnO_2 coating. For this condition, elemental mapping of the CF/MnO_2 showed C elements within and Mn and O elements at the exterior of the fibers, indicating the successful coating of MnO_2 onto the CF substrate.

In contrast, CF/MoO_3 formed a unique bamboo-like architecture of repeating MoO_3 units on the CF substrate with the thinckness and interval distance of *ca*. 1 and 1.5 μm, respectively. The formation mechanism of the bamboo-like architecture can be explained by the competition between the nucleation rate and the growth rate of MoO_3 [34–36]. Because the rapid growth rate outweighed the nucleation rate under the experimental condition of –2.0 V and 70 °C, the laterally grown MoO_3 coating was cracked perpendicular to the axial direction of the CF substrate, which resulted in the bamboo-like structure. However, the formation of extensive cracks along random directions with increasing electrodeposition time led to the destruction of the architecture. Accordingly, the optimal structure of the bamboo-like CF/MoO_3 was obtained at the electrodeposition time of 10 min. The resulting CF/MoO_3 had characteristic elemental compositions of C elements in the interior and Mo and O elements on the exterior of the fibers, which represented the successful growth of MoO_3 on the CF substrate. EDS analysis was also carried out to quantify the CF/MnO_2 and CF/MoO_3 atomic compositions (**Figure 5**). The Mn:O and Mo:O atomic ratios were 1:2 and 1:3, respectively, which corresponded to the atomic composition of MnO_2 and MoO_3.

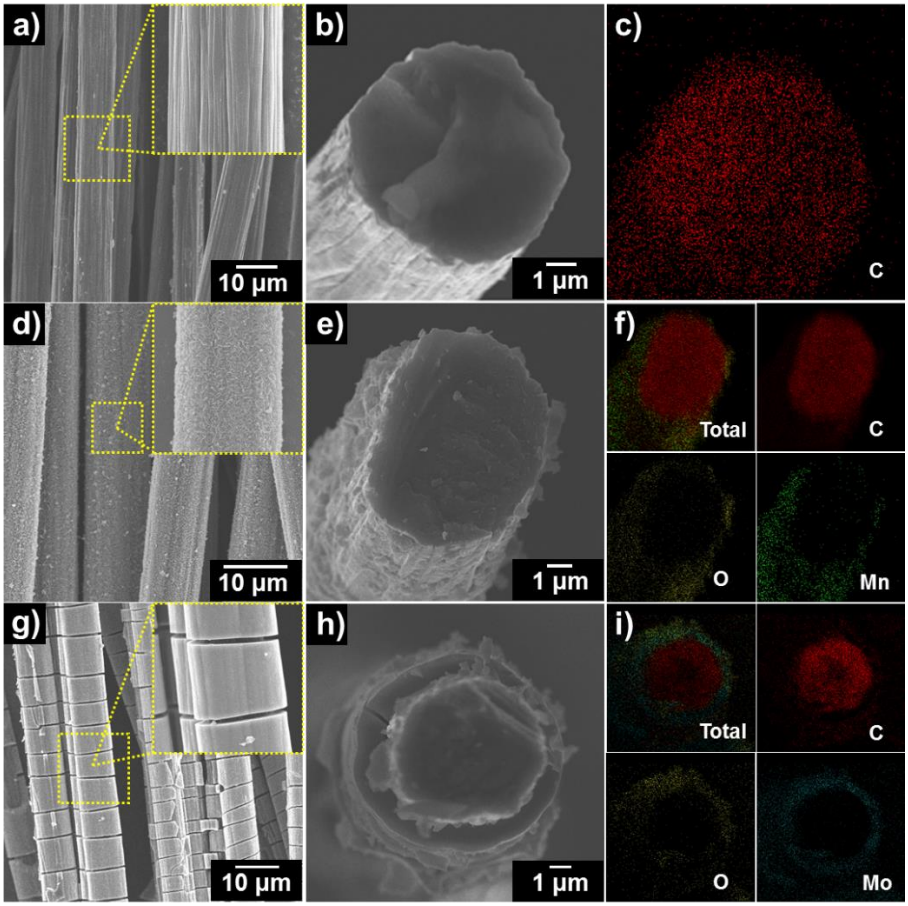

Figure 3. FE-SEM images of (a) CF, (d) CF/MnO_2, and (g) CF/MoO_3 [inset: FE-SEM images with high magnification]. (b, e, h) Cross-sectional FE-SEM images and (c, f, i) elemental mapping of the corresponding samples.

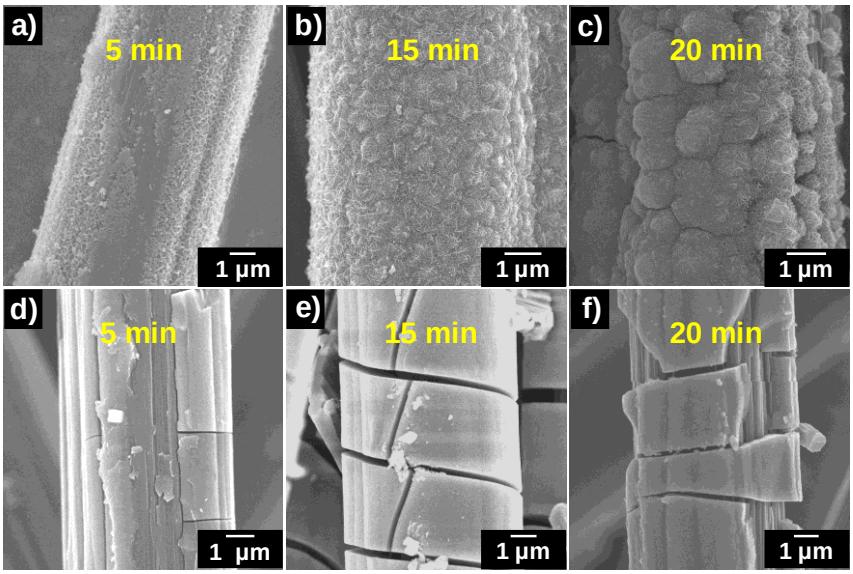

Figure 4. SEM images of CF/MnO_2 and CF/MoO_3 fabricated at different reaction time. (a-c) SEM images of CF/MnO_2 with reaction time of 5, 15, and 20 min, respectively (at constant current of 20 mA and 70°C). (d-f) SEM images of CF/MoO_3 with reaction time of 5, 15, and 20 min, respectively (at constant voltage of –2 V and 70°C).

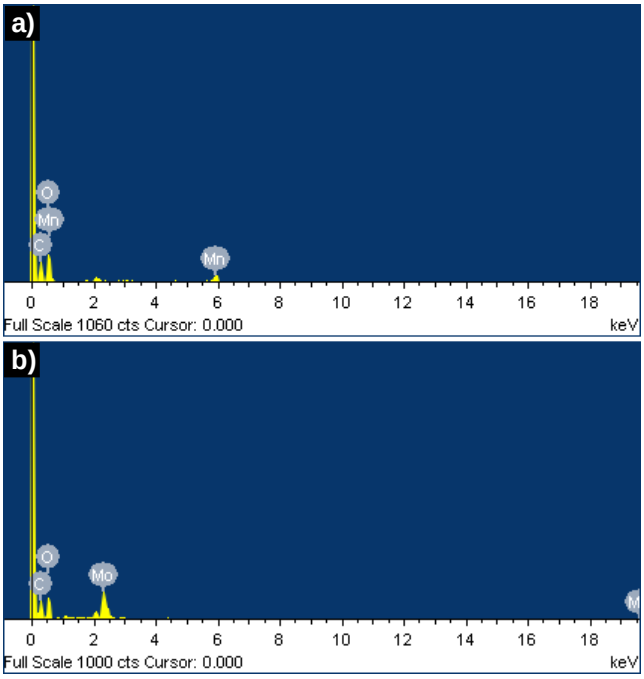

Figure 5. EDS analysis of (a) CF/MnO_2 and (b) CF/MoO_3, respectively.

Table 1. Atomic composition of CF/MnO_2 and CF/MoO_3 active materials.

Materials	Atomic %[a]				
	C	O	Mn	Mo	Total
CF/MnO_2	49.1	34.9	16.0	–	100.0
CF/MoO_3	56.0	33.9	–	10.1	100.0

[a] Atomic percentages of CF/MnO_2 and CF/MoO_3 were measured by FE-SEM (JSM–6700F, JEOL) equipped with an EDS spectrometer (INCA energy).

X-ray photoelectron spectroscopy (XPS) analyses established the chemical states of the CF/MnO_2 and CF/MoO_3 (**Figure 6a–c)**. Wide-scan XPS spectra confirmed the presence of MnO_2 and MoO_3 on the CF substrate. Peaks associated with Mn and Mo were detected for the CF/MnO_2 and CF/MoO_3 in addition to the peaks for elemental C. In particular, the characteristic doublet of Mn^{2+} $2p_{1/2}$ (654.1 eV) and Mn^{2+} $2p_{3/2}$ (642.4 eV) from CF/MnO_2 identified MnO_2 among the various possible manganese oxides [37]. In contrast, the complex mix of peaks observed for the CF/MoO_3 suggested multiple valence states for Mo. For an in-depth interpretation of the MoO_3 spectrum, the peaks at the Mo 3d level were deconvoluted into Mo^{6+} $3d_{3/2}$ (235.7 eV), Mo^{6+} $3d_{5/2}$ (232.6 eV), Mo^{5+} $3d_{3/2}$ (234.3 eV), and Mo^{5+} $3d_{5/2}$ (231.4 eV) peaks [38,39]. A peak at 237.8 eV was also detected that was attributed to the localized charge density of MoO_3, arising from the high-energy beam source [40,41]. The deconvoluted Mo 3d peaks thus confirmed that partially reduced MoO_3 was coated on the CF substrate.

X-ray diffraction (XRD) analysis was used to study the crystallinity of the CF/MnO_2 and CF/MoO_3 (**Figure 6d**). While pristine CF showed only a broad peak at $2\theta = 25.8°$, both CF/MnO_2 and CF/MoO_3 showed additional diffraction peaks. Those of CF/MnO_2 at 2θ = 14.2, 17.1, and 36.6° corresponded to the (110), (200), and (211) planes of tetragonal α-MnO_2, respectively (JCPDS card number 44–0141) [42]. The diffraction peaks of CF/MoO_3 at 2θ = 12.9 23.5, and 27.4° indexed to the (020), (110), and (021) planes, respectively, of

orthorhombic α-MoO_3 (JCPDS card number 05–0508).[43] Hence, various characterizations confirmed the successful decoration of MnO_2 and MoO_3 on the CF substrate.

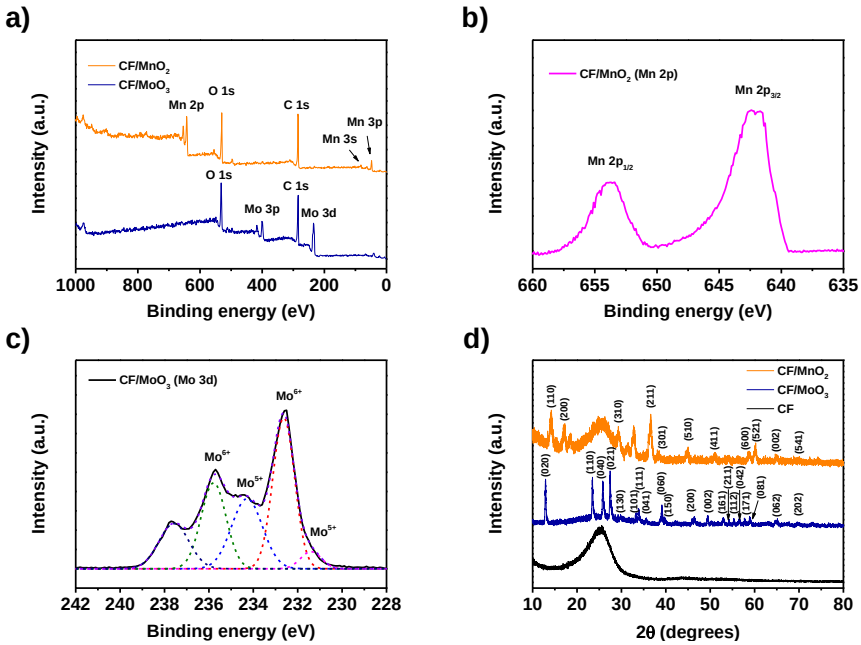

Figure 6. (a) Wide-scan XPS spectra of CF/MnO_2 and CF/MoO_3. XPS spectra of (b) Mn 2p level for CF/MnO_2 and (c) Mo 3d level for CF/MoO_3. (d) XRD patterns of CF/MnO_2, CF/MoO_3, and CF, respectively.

3.2. Electrochemical properties in a three electrode system

The electrochemical properties of CF/MnO_2 and CF/MoO_3 were studied in a three electrode system to evaluate their suitability in energy storage devices. The three electrode configuration was composed of the active materials as working electrodes, Pt wire as a counter electrode, and Ag/AgCl as a reference electrode in a 1 M Na_2SO_4 electrolyte solution. Cyclic voltammetry (CV) curves of the active materials were measured at 50 mV s^{-1} to estimate their operating voltage windows (**Figure 7a**). The electrochemical performance of CF/MnO_2 was measured at a potential ranging from –0.1 to 0.8 V while that of CF/MoO_3 was determined at a potential ranging from –1.0 to 0 V. The different operating voltage windows enabled them to be used as the positive and negative electrodes for supercapacitors.

The CV curves of the active materials were also measured at various scan rates **(Figure 7b–c**). The CF/MnO_2 curves showed a high areal capacitance of 61.1 mF cm^{-2} at a scan rate of 10 mV s^{-1}. However, the curves gradually deviated from the original shape with increasing scan rates, which indicated degradation of the electrochemical performance. In contrast, CV curves of CF/MoO_3 manifested clear redox peaks that were ascribed to the topotactic redox reactions of layered MoO_3, as described by the following equation:

$$xM^+ + xe + yH_2O + MoO_3 \leftrightarrows M_x^+(H_2O)_y[MoO_3]^{x-} \quad (5)$$

where *M* is the metal cation from the electrolytes [44]. During the redox reaction, MoO_3 formed a series of hydrated nonstoichiometric compounds of the types $M_{0.2}^{+}(H_2O)_y[MoO_3]^{0.2-}$, $M_{0.5}^{+}(H_2O)_y[MoO_3]^{0.5-}$, and $M^{+}(H_2O)_y[MoO_3]^{-}$ at the potentials of −0.1, −0.5, and −0.8 V, respectively [45]. Notably, the redox peaks of CF/MoO_3 were maintained even at a scan rate of 200 mV s^{-1}, which suggested that its good rate capability resulted from a fast faradaic reaction [33]. Specifically, CF/MoO_3 showed areal capacitance of 20.3 mF cm^{-2} at a scan rate of 10 mV s^{-1}; 60% of the capacitance was retained as the scan rate was increased to 200 mV s^{-1}.

The galvanostatic charge-discharge (GCD) curves of CF/MnO_2 and CF/MoO_3 at different current densities were collected to further understand the electrochemical properties (**Figure 7d-f)**. The nonlinear GCD curves revealed pseudocapacitive behavior that resulted from the surface-confined faradaic reaction of the active materials [46]. Due to the pseudocapacitive contribution, the areal capacitances of CF/MnO_2 and CF/MoO_3 were 66.4 and 27.5 mF cm^{-2}, respectively, at a current density of 0.5 mA cm^{-2}. Even at a high current density of 5 mA cm^{-2}, the areal capacitances of CF/MnO_2 and CF/MoO_3 retained 33.2 and 16.6 mF cm^{-2}, respectively, which were 50.0 and 60.4% of the original capacitances. The good rate capabilities of the active materials were attributed to the conductive CF substrate that assisted charge transfer of the metal oxides [8,17].

Additionally, various CV curves of CF/MnO_2 and CF/MoO_3 were obtained

to identify the optimal reaction conditions to achieve the highest electrochemical performance (**Figures 9** and **10**). The capacitance values were limited by the cases of either not fully grown or excessively coated metal oxides on the surface of the CF. Initially, the capacitances of the active materials improved with increasing reaction time. However, at long reaction times, excessive self-aggregation of MnO_2 and structural destruction of MoO_3 obstructed the charge transport of the active materials [47,48]. The capacitance of both active materials were maximized at the electrodeposition time of 10 min, at which time morphologies were uniform (**Figure 3)**.

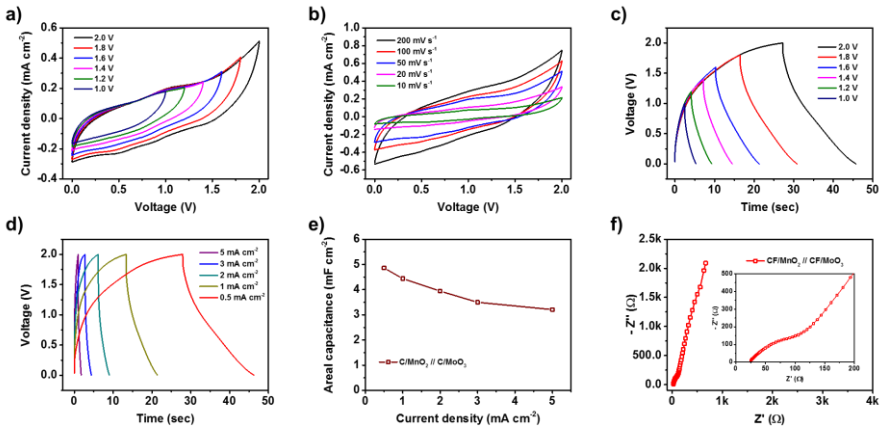

Figure 7. (a) Cyclic voltammetry (CV) curves of the active materials in three electrode system with a scan rate of 50 mV s^{-1}. CV curves of (b) CF/MnO_2 and (c) CF/MoO_3 at various scan rates. Galvanostatic charge-discharge (GCD) curves of (d) CF/MnO_2 and (e) CF/MoO_3 at various current densities. (f) Areal capacitance of the active materials at different current densities.

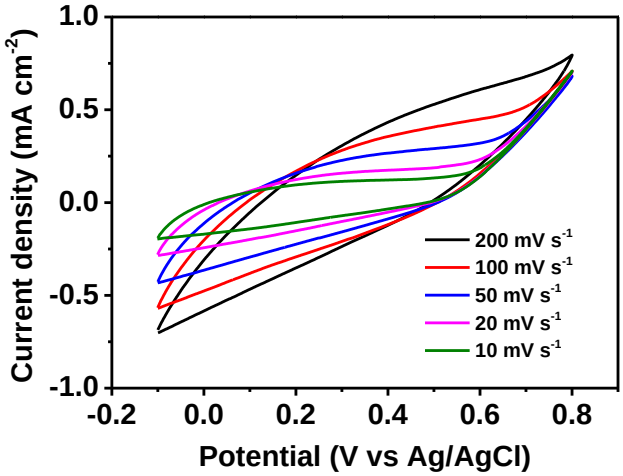

Figure 8. CV curves of carbon fiber (CF) with varying scan rates in three electrode system

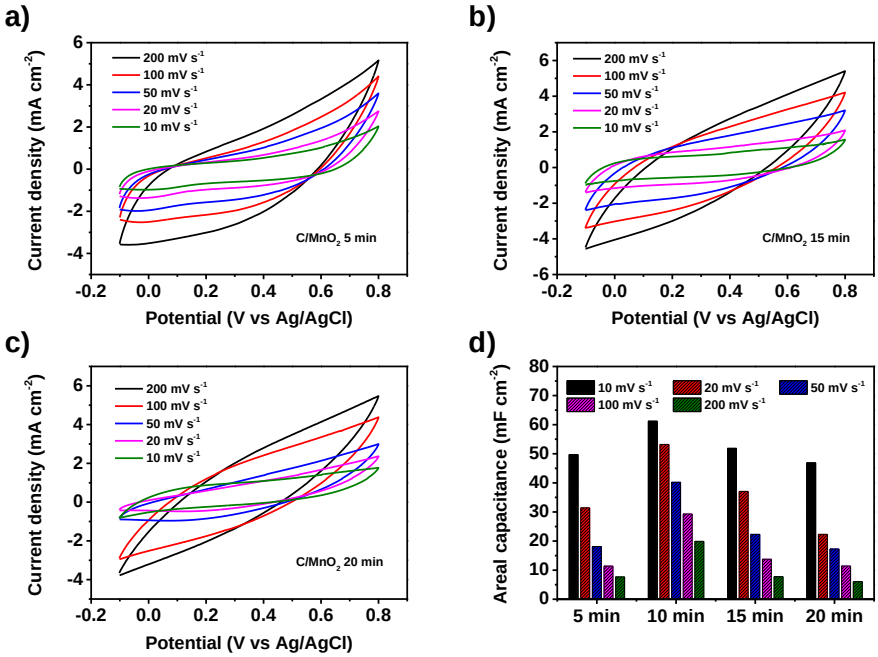

Figure 9. CV curves of CF/MnO_2 electrodes with varying reaction time in three electrode system. CV curves of CF/MnO_2 with reaction time of (a) 5, (b) 15, and (c) 20 min, respectively. (d) Areal capacitance of the various CF/MnO_2 materials.

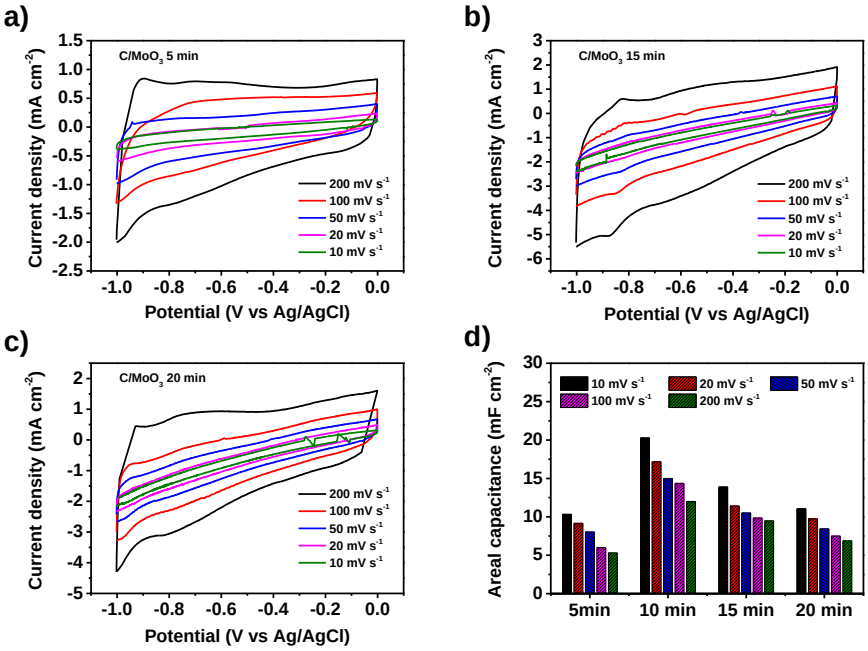

Figure 10. CV curves of CF/MoO_3 electrodes with varying reaction time in three electrode system. CV curves of CF/MoO_3 with reaction time of (a) 5, (b) 15, and (c) 20 min, respectively. (d) Areal capacitance of the various CF/MoO_3 materials.

3.3. Fiber-shaped asymmetric supercapacitor

3.3.1. Construction of the supercapacitor

A fiber-shaped ASC device was fabricated using CF/MnO_2 as the positive electrode and CF/MoO_3 as the negative electrode. The size of the active materials was determined by the charge balance relationship of $Q_+ = Q_-$ where Q_+ is the positive electrode charge and Q_- is the negative electrode charge. The charge storage at each electrode relies on the capacitance (C), operating voltage window (ΔV), and surface area (S), as given by the following equation:[49]

$$Q = C \times \Delta V \times S \tag{6}$$

To satisfy $Q_+ = Q_-$, the areal balance is expressed as the following relationship:[49]

$$\frac{S_+}{S_-} = \frac{C_- \times \Delta V_-}{C_+ \times \Delta V_+} \tag{7}$$

Based on the GCD results of the active materials with the three electrode system, the areal ratio of CF/MnO_2 and CF/MoO_3 was set to 2.4 for the fiber-shaped ASC device. Subsequently, the active materials were separated by PVA/KOH gel electrolyte and twisted to construct the all-solid-state fiber-shaped ASC device.

3.3.2. Electrochemical performance

The CV curves of the assembled ASC device at a scan rate of 50 mV s^{-1} demonstrated that the active materials with a large work function difference widened the operating voltage window to 2.0 V (**Figure 11a**). This was because the operating voltage window is determined by the sum of the work function difference and the surface polarization of positive and negative electrodes [30,50,51]. As the operating voltage window increased from 1.0 to 2.0 V, distinctive anodic peaks appeared due to the pseudocapacitance of the metal oxides. This led to the development of cathodic peaks as the voltage was scanned reverse. Notably, the redox peaks of the ASC device resembled those observed for CF/MoO_3 in the three electrode system. This pseudocapacitive process contributed to the enhancement of the capacitive behavior along with the electric double layer capacitance (EDLC) from the CF substrate. The redox peaks were stably maintained for scan rates ranging from 10 to 200 mV s^{-1} (**Figure 11b)**, and signified the fast ion transport and charge transport properties of the active materials [33,52].

The GCD curves were also used to study the electrochemical performance of the ASC device. The GCD curves demonstrated that the operating voltage window of the ASC device could be increased from 1.0 to 2.0 V (**Figure 11c)**. The slope change in the GCD curves resulted from the redox reactions of the

metal oxides [46,53]. Due to the additional contribution of pseudocapacitive process, the areal capacitance of the ASC device increased as the operating voltage window expanded (**Figure 12**). When the operating voltage window was 2.0 V, the areal capacitance of the ASC device reached 4.86 mF cm^{-2} at a current density of 0.5 mA cm^{-2}. **Figure 12d** presents the GCD curves of the ASC device measured at various current densities ranging from 0.5 to 5 mA cm^{-2}. The electrochemical performance of the ASC device gradually diminished with increasing current density. However, the areal capacitance was 3.20 mF cm^{-2} at a current density of 5 mA cm^{-2}, which indicated good rate capability with a capacitance retention of 65.8% (**Figure 11e**). This remarkable rate capability resulted from the conductive CF substrate, which reduced the electrical resistance of the active materials [8].

The electrochemical properties were further examined by the electrochemical impedance spectroscopy (EIS) (**Figure 11f**). The impedance of the ASC device was tested in the frequency range from 10 mHz to 100 kHz with an alternating current (AC) perturbation of 10 mV. At high frequencies, the electrodes had resistive characteristics that consisted of the equivalent series resistance (ESR) and charge transfer resistance (R_{ct}). ESR corresponds to the total resistance combined with the ionic resistance of the electrolyte, the intrinsic resistance of the substrate, and the contact resistance at the active

material/current collector interface [13,54]. R_{ct} denotes the resistance induced by the faradaic reaction at the interface between the electrode and electrolyte [53,55]. The ASC device had ESR and R_{ct} values of 9.6 and 6.2 Ω, respectively, which derived from the low resistance of the conductive CF substrate and the compact cell assembly. At low frequencies, the ASC device showed capacitive behavior that appeared as a marked increase in the imaginary parts of impedance; a vertical increase generally indicates ideal capacitance [56]. Thus, the EIS measurement indicated that the ASC device had good capacitive behavior.

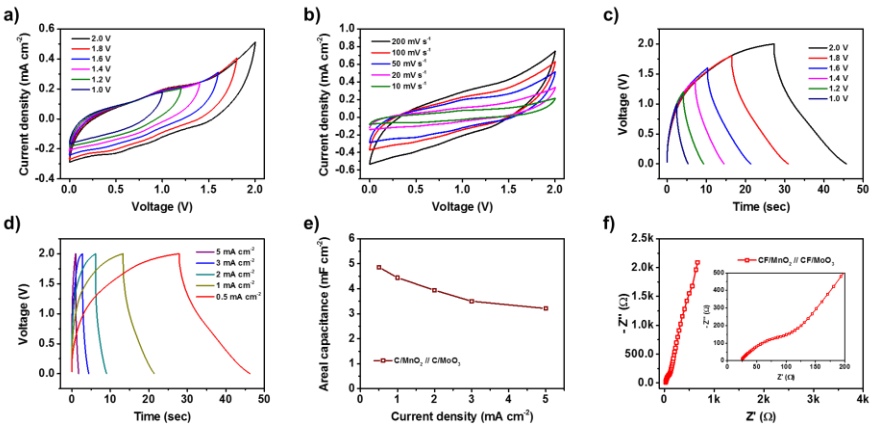

Figure 11. (a-b) CV curves of the assembled all-solid-state fiber-shaped asymmetric supercapacitor (ASC) device with various cell voltages and scan rates. (c-d) GCD curves of the ASC device with different voltage windows and current densities. (e) Areal capacitance of the ASC device with different current densities. (f) Electrochemical impedance spectroscopy (EIS) analysis of the ASC device.

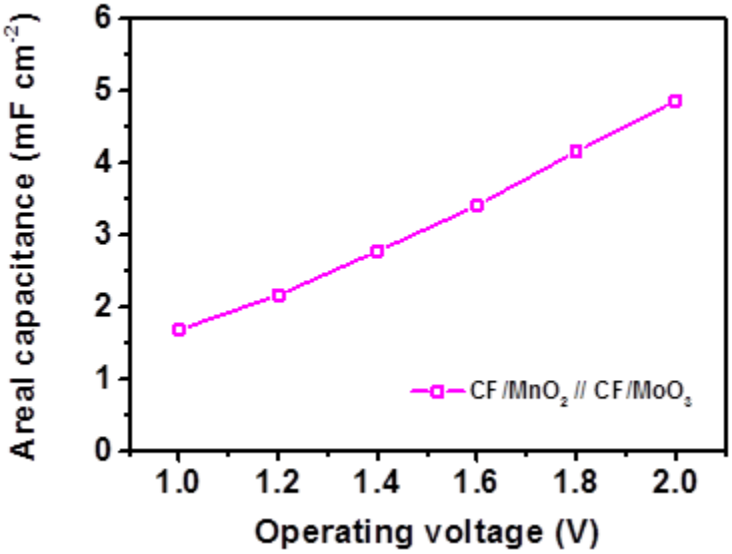

Figure 12. Areal capacitances of the fiber-shaped ASC device with increasing the operating voltage window.

3.3.3. Feasibility test

Figure 13a shows the digital photograph of the assembled all-solid-state fiber-shaped ASC device. As noted above, the commercially available CF substrate was coated by the metal oxides *via* a facile electrodeposition method. The ACS device was constructed by simply twisting the active materials together. Thus, the overall manufacturing procedure is easily applicable to practical energy storage devices. To demonstrate this, we powered a red light-emitting diode (LED) using the ASC device (**Figure 13b**). After charging by applying 2.0 V for 10 min, the ASC device was connected to the 1.6 V red LED. The discharge current from the ACS device flowed through the LED bulb, resulting in successful red light illumination. This feasibility test of the ASC device demonstrated its outstanding performance, which derived from the high capacitance and extended operating voltage window.

Long-term cycling and bending tests were conducted to explore the electrochemical and mechanical stabilities of the ASC device (**Figure 13c–d**). The long-term electrochemical stability was evaluated at a current density of 5 mA cm^{-2} for 3000 cycles. The capacitance of the ASC device retained 89% of its initial value, indicating good cycling stability. The mechanical stability was examined by obtaining CV curves for different bending angles. The pronounced flexibility of the ASC device enabled the CV curves to maintain the original

shape even at the severe bending angles of 90 and 180°. Clearly, the device has great potential for practical energy storage systems due to its facile manufacturing procedure, remarkable performance, and excellent stability.

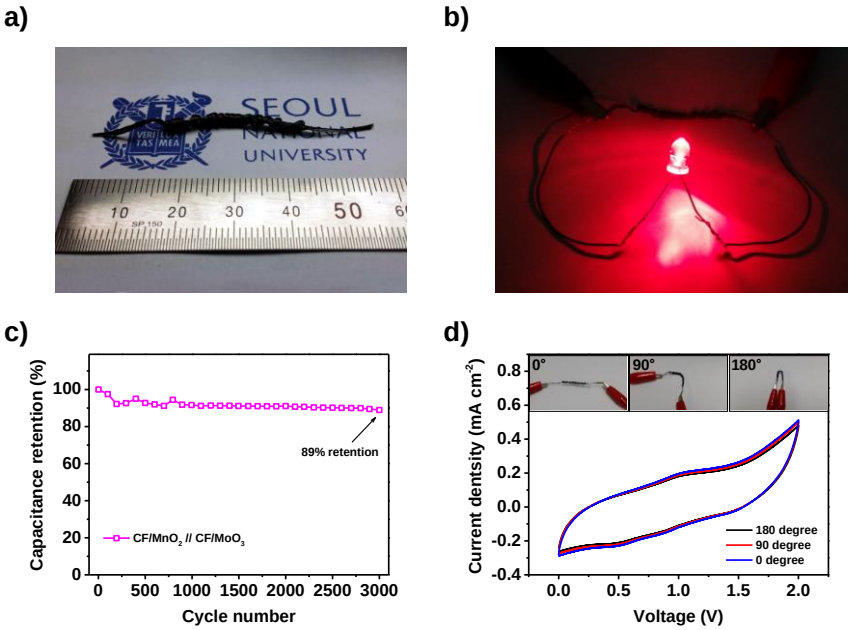

Figure 13. Digital photograph of (a) CF/MnO_2//CF/MoO_3 fiber-shaped ASC device. (b) Photograph of the ASC device lightning red LED. (c) Long-term cycling test of the ASC device with a current density of 5 mA cm^{-2}. (d) CV curves of the ASC device with different bending angles.

3.3.4. Performance evaluation

Efficient energy storage devices are required to provide high energy density without a reduction in power density. Mainly, the wide operating voltage window can play a significant role in improving the electrochemical performance [19, 57]. When each CF/MnO_2 and CF/MoO_3 was constructed as the symmetric supercapacitors, this factor clearly showed its contribution (**Figure 14**). In specific, these symmetric devices assembled by CF/MnO_2 and CF/MoO_3 had the operating voltage windows which were 0.9 V and 1.0 V, respectively. Despite their higher capacitances than the ASC device, these limited operating voltage windows made the symmetric configuration deliver the lower energy density and power density. Thus, our design of the ASC device was proved to be a powerful way to improve the electrochemical performance. **Figure 15** compares the energy density and power density of the fiber-shaped ASC device with those of other fiber-based supercapacitors [57-64]. At a current density of 0.5 mA cm^{-2}, the energy density reached a maximum value of 2.70 μWh cm^{-2} with a power density of 0.53 mW cm^{-2}. As the current density was increased to 5 mA cm^{-2}, the energy density of the ASC device decreased to 1.78 μWh cm^{-2} while the power density increased to 8.30 mW cm^{-2}. Sufficiently high energy density was delivered even at a high power density, which demonstrated the efficient performance of the ASC device. These values

are higher than for many fiber-based supercapacitors, and are attributed to the reduced resistance, high areal capacitance, and extended operating voltage window. Therefore, the fiber-shaped ASC device based on CF/MnO_2 and CF/MoO_3 exhibited superior performance and showed considerable promise for energy storage applications.

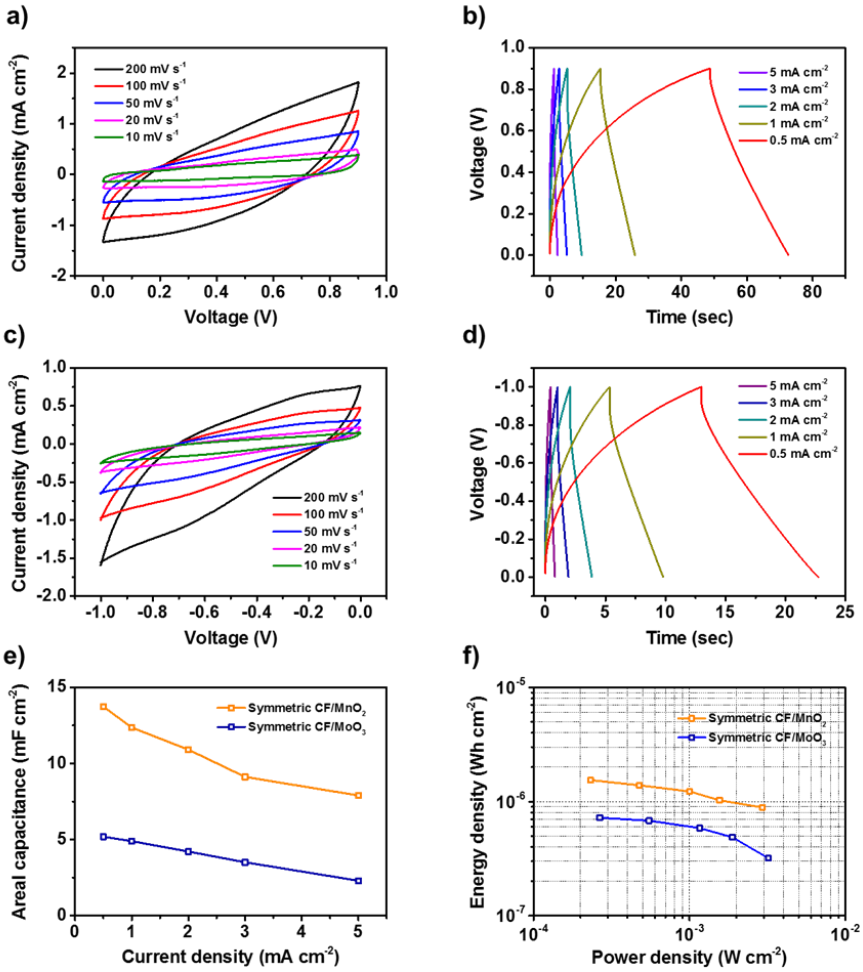

Figure 14. (a, b) Cyclic voltammetry (CV) and galvanostatic charge discharge (GCD) curves of the symmetric supercapacitor assembled by CF/MnO_2. (c, d) CV and GCD curves of the symmetric supercapacitor constructed by CF/MoO_3. (e, f) The areal capacitance and Ragone plot of the symmetric supercapacitors.

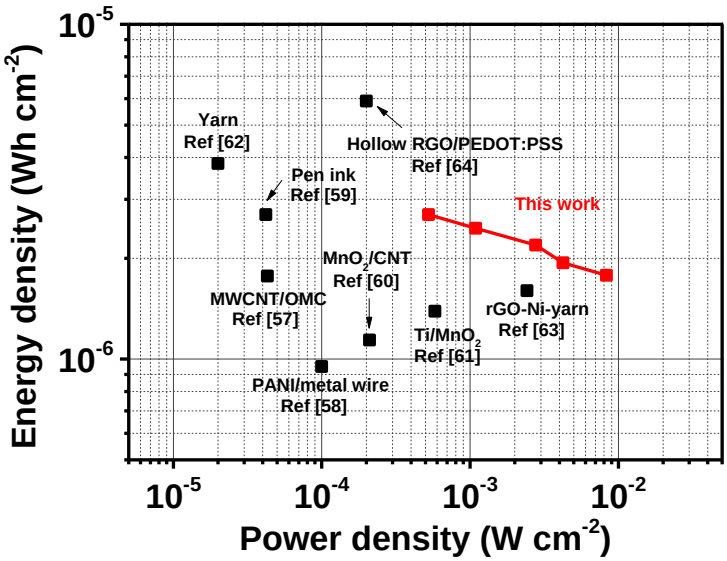

Figure 15. Ragone plot of CF/MnO_2//CF/MoO_3 fiber-shaped ASC device compared to various fiber-based supercapacitor devices.

Chapter 4. Conclusion

In summary, we fabricated CF/MnO_2 and CF/MoO_3 active materials using a simple electrodeposition method and used them to construct a high-performance, fiber-shaped ASC device. The active materials, with their large work function difference, provided remarkable electrochemical performance to the ASC device. In particular, the large work function difference enlarged the operating voltage window of the ASC device to 2.0 V. The maximum areal capacitance of the ASC reached 4.86 mF cm^{-2} at a current density of 0.5 mA cm^{-2}. As the current density increased to 5 mA cm^{-2}, the areal capacitance retained 65.8% of its initial value, indicating good rate capability. Such a wide operating voltage window and high capacitance resulted in the remarkable energy density and power density, i.e., 2.70–1.78 μWh cm^{-2} and 0.53–8.30 mW cm^{-2}, respectively. Notably, the ASC device delivered a high energy density without a significant decrease in the power density. The outstanding energy density and power density were better than those of many fiber-based supercapacitors. Moreover, long-term cycling and bending tests revealed excellent electrochemical and mechanical stabilities, implying the good endurance under harsh operating conditions. The excellent performance of the ASC device holds promise for fiber-shaped energy storage devices.

References

[1] Z. Liu, J. Xu, D. Chen, G. Shen, *Chem. Soc. Rev.* **2015**, *44*, 161.

[2] B. C. Kim, J. Hong, G. G. Wallace, H. S. Park, *Adv. Energy Mater*. **2015**, *5*, 1500959.

[3] X. Wang, X. Lu, B. Liu, D. Chen, Y. Tong, G. Shen, *Adv. Mater.* **2014**, *26*, 4763.

[4] X. Lu, M. Yu, G. Wang, Y. Tong, Y. Li, *Energy Environ. Sci.* **2014**, *7*, 2160.

[5] L. Li, Z. Wu, S. Yuan, X. Zhang, *Energy Environ. Sci.* **2014**, *7*, 2101.

[6] M. Kim, C. Lee, J. Jang, *Adv. Funct. Mater.* **2014**, *24*, 2489.

[7] G. Sun, X. Zhang, R. Lin, J. Yang, H. Zhang, P. Chen, *Angew. Chem.* **2015**, *127*, 4734.

[8] N. Yu, H. Yin, W. Zhang, Y. Liu, Z. Tang, M. Zhu, *Adv. Energy Mater*. **2016**, *6*, 1501458.

[9] S. Pan, H. Lin, J. Deng, P. Chen, X. Chen, Z. Yang, H. Peng, *Adv. Energy Mater*. **2015**, *5*, 1401438.

[10] Z. Yang, J. Deng, X. Chen, J. Ren, H. Peng, *Angew. Chem. Int. Ed.* **2013**, *52*, 13453.

[11] J. Ren, L. Li, C. Chen, X. Chen, Z. Cai, L. Qiu, Y. Wang, X. Zhu, H. Peng, *Adv. Mater.* **2013**, *25*, 1155.

[12] A. Lamberti, A. Gigot, S. Bianco, M. Fontana, M. Castellino, E. Tresso, C. F. Pirri, *Carbon* **2016**, *105*, 649.

[13] J. S. Lee, D. H. Shin, J. Jang, *Energy Environ. Sci.* **2015**, *8*, 3030.

[14] C. Y. Foo, A. Sumboja, D. J. H. Tan, J. Wang, P. S. Lee, *Adv. Energy Mater*. **2014**, *4*, 1400236

[15] H. Xia, C. Hong, B. Li, B. Zhao, Z. Lin, M. Zheng, S. V. Savilov, S. M. Aldoshin, *Adv. Funct. Mater.* **2015**, *25*, 627.

[16] C. Long, D. Qi, T. Wei, J. Yan, L. Jiang, Z. Fan, *Adv. Funct. Mater*. **2014**, *24*, 3953.

[17] P. Yang, Y. Ding, Z. Lin, Z. Chen, Y. Li, P. Qiang, M. Ebrahimi, W. Mai, C. P. Wong, Z. L. Wang, *Nano Lett.* **2014**, *14*, 731.

[18] J. W. Park, W. Na, J. Jang, *J. Mater. Chem. A.* **2016**, *4*, 8263.

[19] R. R. Salunkhe, J. Tang, Y. Kamachi, T. Nakato, J. H. Kim, Y. Yamauchi, *ACS Nano* **2015**, *9*, 6288.

[20] Y. Zhao, W. Ran, J. He, Y. Huang, Z. Liu, W. Liu, Y. Tang, L. Zhang, D. Gao, F. Gao, *Small* **2015**, *11*, 1310.

[21] Z. Yu, J. Moore, J. Calderon, L. Zhai, J. Thomas, *Small* **2015**, *11*, 5289.

[22] S. Cho, M. Kim, J. Jang, *ACS Appl. Mater. Interfaces* **2015**, *7*, 10213.

[23] G. Yu, L. Hu, N. Liu, H. Wang, M. Vosgueritchian, Y. Yang, Y. Cui, Z. Bao, *Nano Lett.* **2011**, *11*, 4438.

[24] H. Xia, C. Hong, X. Shi, B. Li, G. Yuan, Q. Yao, J. Xie, *J. Mater. Chem. A*, **2015**, *3*, 1216.

[25] X. Xiao, T. Li, P. Yang, Y. Gao, H. Jin, W. Ni, W. Zhan, X. Zhang, Y. Cao, J. Zhong, L. Gong, W. Yen, W. Mai, J. Chen, K. Huo, Y. Chueh, Z. L. Wang, J. Zhou, *ACS Nano* **2012**, *6*, 9200.

[26] B. Liu, D. Tan, X. Wang, D. Chen, G. Shen, *Small* **2013**, *9*, 1998.

[27] M. Yu, X. Cheng, Y. Zeng, Z. Wang, Y. Tong, X. Lu, S. Yang, *Angew. Chem. Int. Ed.* **2016**, *55*, 6762.

[28] B. Mendoza-Sanchez, T. Brousse, C. Ramirez-Castro, V. Nicolosi, P. S. Grant, *Electrochimica Acta* **2013**, *91*, 253.

[29] X. Xiao, T. Ding, L. Yuan, Y. Shen, Q. Zhong, X. Zhang, Y. Cao, B. Hu, T. Zhai, L. Gong, J. Chen, Y. Tong, J. Zhou, Z. L. Wang *Adv. Energy Mater.* **2012**, *2*, 1328.

[30] J. Chang, M. Jin, F. Yao, T. H. Kim, V. T. Le, H. Yue, F. Gunes, B. Li, A. Ghosh, S. Xie, Y. H. Lee, *Adv. Funct. Mater.* **2013**, *23*, 5074.

[31] M. T. Greiner, M. G. Helander, W. Tang, Z. Wang, J. Qiu, Z. Lu, *Nat. Mater.* **2012**, *11*, 76.

[32] Z. Yu, B. Duong, D. Abbitt, J. Thomas, *Adv. Mater.* **2013**, *25*, 3302.

[33] Q. Lv, S. Wang, H. Sun, J. Luo, J. Xiao, J. Xiao, F. Xiao, S. Wang, *Nano Lett.* **2016**, *16*, 40.

[34] T. Ressler, R. E. Jentoft, J. Wienold, M. M. Gü1nter, O. Timpe, *J. Phys. Chem. B* **2000**, *104,* 6360.

[35] T. Vetter, M. Iggland, D. R. Ochsenbein, F. S. Hanseler, M Mazzotti, *Cryst. Growth Des.* **2013**, *13*, 4890.

[36] A. Chithambararaj, N. R. Yogamalar, A. C. Bose, *Cryst. Growth Des.* **2016**, *16*, 1984.

[37] B. G. Choi, M. Yang, W. H. Hong, J. W. Choi, Y. S. Huh, *ACS Nano* **2012**, *6*, 4020.

[38] R. B. Quincy, M. Houalla, A. Proctor, D. M. Hercules, *J. Phys. Chem.* **1990**, *94*, 1520.

[39] P. Wang, Y. Lo, W. Tseng, M. Chen, C. Wu, *Appl. Phys.* **2013**, *114*, 063710.

[40] B. Nagy, D. Ábrahám, G. Dobos, J. Madarász, G. Onyestyák, G. Sáfrán, E. Geissler, K. László, *Carbon* **2014**, *66*, 210.

[41] S. F. Ho, S. Contarini, J. W. Rabalais, *Chem. Phys. Lett.* **1987**, *133*, 171.

[42] Z. Li, Y. Ding, Y. Xiong, Q. Yang, Y. Xie, *Chem. Commun*. **2005**, *7*, 918.

[43] X. W. Lou, H. C. Zeng, *Chem. Mater.* **2002,** *14*, 4781.

[44] R. Schöllhorn, *Angew. Chem. Int. Ed. Engl.* **1980**, *19*, 983.

[45] L. Huang, X. Gao, Q. Dong, Z. Hu, X. Xiao, T. Li, Y. Cheng, B. Yao, J. Wan, D. Ding, Z. Ling, J. Qiub, J. Zhou, *J. Mater. Chem. A* **2015**, *3*, 17217.

[46] G. S. Gund, D. P. Dubal, N. R. Chodankar, J. Y. Cho, P. Gomez-Romero, C. Park, C. D. Lokhande, *Scientific Reports* **2015**, *5*, 12454.

[47] Y. Jin, H. Chen, M. Chen, N. Liu, Q. Li, *ACS Appl. Mater. Interfaces* **2013**, *5*, 3408.

[48] H. Chen, L. Hu, M. Chen, Y. Yan, L. Wu, *Adv. Funct. Mater.* **2014**, *24*, 934.

[49] J. Yan, Z. Fan, W. Sun, G. Ning, T. Wei, Q. Zhang, R. Zhang, L. Zhi, F. Wei, *Adv. Funct. Mater.* **2012**, *22*, 2632.

[50] J. Cheng, M. Sprik, *Phys. Chem. Chem. Phys.* **2012**, *14*, 11245.

[51] S. Trasátti, *Pure Appl. Chem.* **1986**, *58*, 955.

[52] Q. Mahmood, M. G. Kim, S. Yun, S. Bak, X. Yang, H. S. Shin, W. S. Kim, P. V. Braun, H. S. Park, *Nano Lett.* **2015**, *15*, 2269.

[53] S. Kim, Y. K. Kim, H. Lee, S. B. Lee, H. S. Park, *ChemSusChem* **2014**, *7*, 1094.

[54] J. S. Lee, D. H. Shin, J. Jun, C. Lee, J. Jang, *ChemSusChem* **2014**, *7*, 1676.

[55] J. Jun, J. S. Lee, D. H. Shin, S. G. Kim, J. Jang, *Nanoscale* **2015**, *7*, 16026.

[56] J. Wang, Y. Yang, Z. Huang, F. Kang, *Journal of Power Sources* **2013**, *224*, 86.

[57] J. Ren, W. Bai, G. Guan, Y. Zhang, H. Peng, *Adv. Mater.* **2013**, *25*, 5965.

[58] Y. Fu, H. Wu, S. Ye, X. Cai, X. Yu, S. Hou, H. Kafafy, D. Zou, *Energy*

Environ. Sci. **2013**, *6*, 805.

[59] Y. Fu, X. Cai, H. Wu, Z. Lv, S. Hou, M. Peng, X. Yu, D. Zou, *Adv. Mater.* **2012**, *24*, 5713.

[60] P. Xu, B. Wei, Z. Cao, J. Zheng, K. Gong, F. Li, J. Yu, Q. Li, W. Lu, J. Byun, B. Kim, Y. Yan, T. Chou, *ACS Nano* **2015**, *9*, 6088.

[61] X. Pu, L. Li, M. Liu, C. Jiang, C. Du, Z. Zhao, W. Hu, Z. L. Wang, *Adv. Mater.* **2016**, *28*, 98.

[62] L. Kou, T. Huang, B. Zheng, Y. Han, X. Zhao, K. Gopalsamy, H. Sun, C. Gao, *Nat. Commun.* **2014**, *5*, 3754.

[63] K. Guo, Y. Ma, H. Li, T. Zhai, *Small* **2016**, *12*, 1024.

[64] G. Qu, J. Cheng, X. Li, D. Yuan, P. Chen, X. Chen, B. Wang, H. Peng, *Adv. Mater.* **2016**, *28*, 3646.

초 록

섬유형 슈퍼캐패시터는 미래의 휘어지고 휴대가능한 전자기기를 위한 전망 받는 에너지 저장 소재이다. 본 논문에서는 최초로 큰 일함수 차이를 지니는 금속산화물들을 휘어질 수 있고 전도성이 있는 카본 섬유에 직접 도입함으로써 섬유형의 비대칭 슈퍼캐패시터를 보고한다. 간단한 전기도금방법을 통해서 카본 섬유/이산화망간과 카본 섬유/삼산화몰리브데늄의 전극을 제조하고, 이를 각각 전고상 섬유형 비대칭 슈퍼캐패시터의 양극과 음극으로 구성하였다. 금속산화물들 간의 큰 일함수 차이와 카본 섬유의 높은 전도성 덕분에 슈퍼캐패시터의 전기화학적 성능을 극대화할 수 있었다. 구체적으로 4.86 mF cm^{-2}의 캐패시턴스와 더불어 2.0 V 라는 넓은 전압 구동 범위를 이끌어 낼 수 있었으며, 이에 해당하는 에너지 밀도와 출력 밀도는 각각 2.70 μWh cm^{-2} 와 0.53 mW cm^{-2} 에 이르렀다. 또한 이러한 성질은 3000 번의 전기화학적 성능 테스트와 기계적 변형에도 견딜 수 있었다. 따라서 섬유형 비대칭 슈퍼캐패시터의 이와 같은 높은 성능과

안정성은 미래의 에너지 저장소재로서의 큰 가능성을 보여준다.

주요어 : 섬유형 슈퍼캐패시터, 비대칭 슈퍼캐패시터, 일함수, 이산화망간, 삼산화몰리브데늄

학번 : 2015-21018

Flexible Asymmetric Supercapacitor Twisted from Carbon Fiber/MnO_2 and Carbon Fiber/MoO_3

지도 교수 장 정 식

이 논문을 공학석사 학위논문으로 제출함

2016 년 12 월

서울대학교 대학원

화학생물공학부

노 정 철

노정철의 석사 학위논문을 인준함

2017 년 1 월

위 원 장 조 재 영 (인)

부위원장 장 정 식 (인)

위 원 이 종 찬 (인)